On the Multipole Vortex (MpV) Motion in a Circular-Port Hybrid Rocket Engine

Mitchell E. Sisk* and Joseph Majdalani†
Auburn University, Auburn, AL 36849

This study focuses on the topology of a Multipole Vortex (MpV) flowfield within a simulated, right-cylindrical hybrid rocket engine. This is accomplished by extending the analysis of the Quardrupole Vortex (QpV) concept developed in previous work to multipole flow configurations. Inspired by the diamond-impregnated tricone roller bits that are used in the oil-extraction industry, an MpV operates as a highly-abrasive fluid mechanical drill that stands to increase combustion efficiency and fuel regression rates in hybrid rocket engines. This is achieved by enhancing mixing between hot combustion products in the core region and the turbulent boundary layer above the grain surface; the resulting flowfield helps to extend particle residence times while providing more precise control over equivalence ratios. These effects contribute to a more stable and predictable swirl-driven hybrid flowfield. In this work, we explore various design configurations with increasing sets of vortices. Using MATLAB and ANSYS simulations, we examine the flow topology associated with four, six, and eight vortices. The complex potential function, which is based on the Milne-Thomson Circle Theorem, is used to derive a compact representation of the mean flow. The study also analyzes equilibrium points and stability characteristics of various configurations using CFD simulations to help verify the analytical predictions. Our results demonstrate that increasing the number of vortices alters equilibrium positions, impacts stability, and affects localized regression rates. By bringing the hot core combustion products in contact with the fuel grain, the intercoiling MpV interactions help to increase the propellant burning flame temperature relative to a cyclonic Vortex Injection Hybrid Rocket Engine. As such, it increases the grain regression rate by more than 120 percent while suppressing potential instabilities and improving the engine's overall propulsive performance.

I. Introduction

HYBRID rocket engines are distinguished by their physical separation of fuel and oxidizer ingredients, wherein the former is typically stored in solid form whereas the latter is introduced in liquid or gaseous phase. This bipropellant configuration offers several technological advantages such as inherent simplicity, reliability, and cost-effectiveness. By requiring only half of the plumbing and turbomachinery of a conventional liquid rocket, hybrid engines eliminate the complexity associated with cryogenic handling and injector atomization while retaining the throttling and restart capabilities. Furthermore, unlike solid rockets, hybrid engines exhibit a self-limiting combustion process that mitigates the risk of catastrophic failures in the event of a mishap. Their propellants, when stored separately, remain chemically inert, thereby ensuring enhanced safety during manufacturing, storage, and operation.

Despite their numerous advantages, hybrid rockets have traditionally exhibited performance limitations relative to their solid and liquid propellant counterparts. While the specific impulse of hybrid engines is generally intermediate between that of solids and liquids, well-designed hybrid systems can approach the performance of bipropellant combinations such as LOX-RP1 [1]. Hybrid propulsion systems also exhibit favorable storability characteristics, as their solid fuel components are non-volatile and impervious to freezing or boil-off under cryogenic conditions. These properties make hybrids particularly attractive for long-duration interplanetary missions, where reducing inert mass and minimizing auxiliary power requirements contribute directly to payload capacity and maneuverability [2]. The intrinsic safety of hybrid propulsion has also positioned it as a preferred choice for academic research, STEM outreach, and sounding rocket applications.

One of the primary limitations of hybrid rockets stems from their diffusion-limited combustion mechanism that unfolds at the interface between the oxidizer and the solid fuel. This fundamental constraint has historically led to four principal deficiencies: (i) low combustion efficiency, (ii) slow fuel regression rate, (iii) reduced volumetric propellant loading, and (iv) susceptibility to combustion instabilities [3]. Unlike the premixed burning of solid or liquid engines, hybrid combustion is prescribed by convective heat transfer from the flame zone to the fuel surface, thus resulting in regression rates that are typically one order of magnitude lower than those associated with solid propellants [4].

To offset these intrinsic limitations, traditional hybrid rockets have relied on multi-port grain matrices that are housed within high-pressure casings. By increasing the available burning surface, these configurations also introduce

*Graduate Research Assistant, Department of Aerospace Engineering. Member AIAA.
†Professor and Francis Chair, Department of Aerospace Engineering. Fellow AIAA.

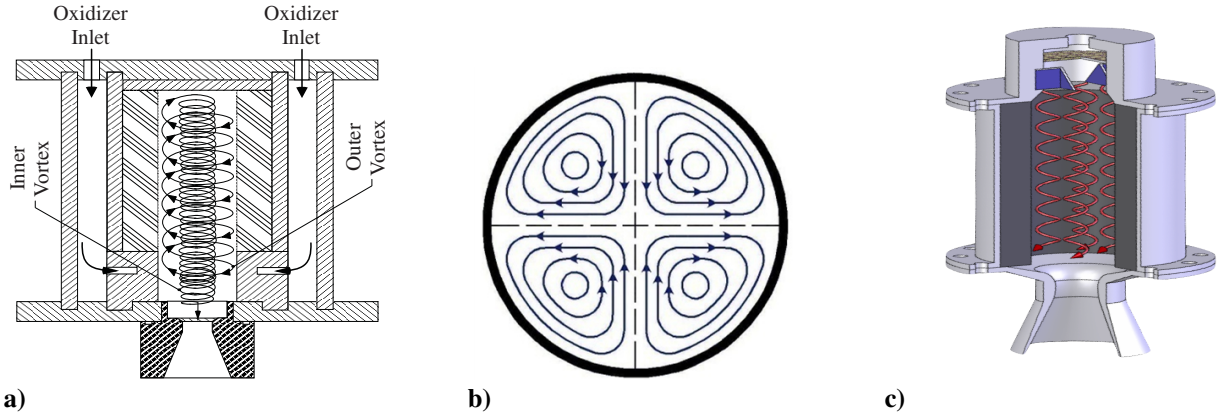

Fig. 1. Schematics of a) Sierra Space's Vortex Injection Hybrid Rocket Engine (VIHRE) by Knuth et al. [9]. Also shown are b) quad vortices with common downwash inside c) a conceptual quadrupole vortex (QpV) engine.

additional dead weight and complexity while leading to incomplete fuel consumption and increased residual slivers. Such underlying inefficiencies have historically hindered the adoption of large-scale hybrid engines for primary launch vehicle stages, as exemplified by the American Rocket Company (AMROC). The latter sought to commercialize hybrid boosters but ultimately ceased operations before achieving full-scale production.

Through continual advances in grain composition and flow configurations, these longstanding impediments to hybrid propulsion have begun to dissipate. Two primary innovations have driven this progress. The first relates to the fast-burning paraffin-based fuels, such as those developed by the Space Propulsion Group [5]. The second major innovation has been the implementation of swirling oxidizer injection and other vortex-driven flowfields that enhance combustion efficiency and fuel regression by intensifying species mixing and heat transfer [6–8].

Of particular relevance to this study is the Vortex Injection Hybrid Rocket Engine (VIHRE), developed by Knuth et al. [9] in the mid nineties, and featured here in Fig. 1a. The VIHRE concept relies on a bidirectional vortex flowfield that substantially enhances combustion efficiency [4, 9]. As confirmed through live tests, VIHRE can achieve regression rates up to seven times higher than those of conventional hybrid engines[6, 10–12]. The principal mechanism underlying VIHRE and other vortex-assisted hybrid engines [13, 14] entails the introduction of a cyclonically swirling oxidizer stream, which increases shear forces at the fuel surface while promoting mass entrainment and burning rate augmentation. Despite these improvements, however, vortex-driven hybrid rockets have been shown to suffer from a fundamental limitation: centrifugal forces drive colder and heavier products outward, and these tend to form a cool gas layer directly above the fuel surface. The latter serves to reduce the flame temperature while impeding the heat transfer to the fuel surface, both being detrimental to the grain regression rate.

To overcome this limitation in part, the present study introduces the Multipole Vortex (MpV) Hybrid Rocket Engine, a novel concept that is intended to optimize surface combustion through the generation of multiple swirling vortex pairs [15]. The MpV engine architecture leverages four, six, or eight columnar vortices that span the length of a simple to manufacture, right-cylindrical chamber. In this context, both theoretical analyses [16] and experimental studies [17, 18] confirm that multipole vortex systems can substantially enhance convective heat transfer in confined flow environments. Fundamentally, this interwoven vortex architecture is anticipated to enhance mixing between the wall boundary layer and the main axial flow. Moreover, the continuous circulatory motion that transports vaporized fuel into the hot, turbulent core can serve to draw high-temperature gases toward the fuel surface. Unlike the VIHRE concept, where a cool oxidizer is swirled along the chamber wall while hot products remain confined to the core, the multipole vortex structure allows for a more uniform thermal distribution and improved reactant mixing.

Naturally, by increasing the flame temperature and thermal energy transport at the fuel surface, the MpV mechanism can induce an order-of-magnitude improvement in regression rate relative to conventional hybrid designs. To show this, the present study will seek to establish a foundational framework for understanding MpV dynamics through analytical modeling and numerical verification, thereby assessing its potential to advance hybrid rocket propulsion. For the reader's convenience, schematics of a Quadrupole Vortex (QpV) motion and its engine concept are provided in Figs. 1b and 1c. The QpV configuration consists of the simplest MpV engine with four internally generated vortices [15].

II. Multipole Vortex (MpV) Flow Formulation

A. Complex Potential and Stream Functions

The starting point of this analysis is a description of the complex potential function used to derive the multipole flowfield in a polar plane. The analysis is launched by assuming that the vortices induced at the head end of the engine do not affect the streamwise velocity component, i.e., that the flow has a transversely-uniform velocity component u_z in the z-direction. This one-way coupling assumption simplifies the analysis by locating all of the meaningful motion in the z-plane, particularly, in the vicinity of the engine headwall region. Figure 2 illustrates the relevant geometry and coordinate system, showing the axes used in the upcoming analysis [15].

To proceed, we follow algebraic tradition and allow z to also represent a variable in the complex plane. With u_x and u_y denoting the real and imaginary parts of the solution in the xy plane, the analysis can be further simplified by permitting the use of the complex potential function in conjunction with the Milne-Thomson Circle Theorem. Proceeding in this manner also yields the benefit of collapsing the two velocity components into a single variable, which proves convenient when implementing the results of this analysis using a numerical solver over a mesh of grid points. By letting $z = x + iy$, the complex potential $f(z) \equiv \phi + i\psi$ for a point vortex located at z_n may be expressed according to the Milne-Thomson Theorem [19] using $f(z) = ik\ln(z - z_n)$, where the vortex strength, $2\pi k \equiv \Gamma = \pi r_R^2 \omega$, may be defined in terms of the flow circulation, Γ, or, alternatively, the core radius, r_R, and the solid-body angular speed, ω, of the forced vortex core.

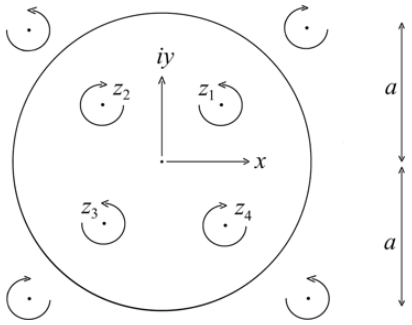

Fig. 2. Coordinate system in a z-plane.

According to the Milne-Thomson Circle Theorem, when the complex potential of an inviscid, incompressible motion with no boundaries is given by $f(z)$, the introduction of a circular-port cylinder of radius a normal to the z-plane gives rise to a new complex potential within the boundary of the cylinder such that $F(z) = f(z) + \overline{f}(a^2/z)$. Accordingly, $\overline{f}$ denotes the conjugate of f. Finally, from the definitions of the stream function, potential function, and complex potential, we may set $\mathrm{d}F/\mathrm{d}z = -u_x + iu_y$. This enables us to readily deduce a mean flow expression for the velocity field once the complex potential becomes available.

B. Potential Flow Reconstruction

Although the foregoing technique may be used to model any number of vortices, it will be focused on the complex potential of a motion consisting of an even number of vortices, N, with vortices that are anchored at axisymmetric points, z_1, z_2, ..., and z_N. We are particularly interested in the special cases corresponding to stable quadrupoles, hexapoles, and octopoles, namely, those arising for $N = 4, 6$, and 8. The solution may be synthesized using the concept of superposition, specifically,

$$f(z) = \sum_{n=1}^{N} ik_n \ \ln(z - z_n) = ik_1 \ln(z - z_1) + ik_2 \ln(z - z_2) + \cdots + ik_N \ln(z - z_N)\,. \tag{1}$$

Then based on the Milne-Thomson Circle Theorem, the complex potential for N vortices enclosed by a circular boundary with radius a may be represented by

$$F(z) = \sum_{n=1}^{N} ik_n \ \ln(z - z_n) - ik_n \ \ln\left(z - a^2/\overline{z_n}\right) = ik_1 \ln(z - z_1) - ik_1 \ln\left(z - a^2/\overline{z_1}\right)$$
$$+ ik_2 \ln(z - z_2) - ik_2 \ln\left(z - a^2/\overline{z_2}\right) + \cdots + ik_N \ln(z - z_N) - ik_N \ln\left(z - a^2/\overline{z_N}\right). \tag{2}$$

At this juncture, the determination of explicit expressions for the axial and normal velocity components will depend on the differentiation and separation of both real and imaginary parts of Eq. (2). This process may be carried out in either order, with the first operation being less labor intensive than the other. For example, differentiating Eq. (2) yields

$$iu_y - u_x = \frac{\mathrm{d}(\phi + i\psi)}{\mathrm{d}z} = \frac{\mathrm{d}F(z)}{\mathrm{d}z} = \frac{ik_1}{z - z_1} - \frac{ik_1}{z - a^2/\overline{z_1}} + \frac{ik_2}{z - z_2} - \frac{ik_2}{z - a^2/\overline{z_2}} + \cdots + \frac{ik_N}{z - z_N} - \frac{ik_N}{z - a^2/\overline{z_N}}. \tag{3}$$

Equation (3) may be relegated to a symbolic program or evaluated numerically for the real and imaginary parts of the right-hand-side fractional members. In our case, explicit expressions for the velocity components and their potential function can be analytically extracted. By temporarily writing the complex numbers in modulus-amplitude form, the real parts may be deduced from the corresponding logarithm [15]. The resulting velocity potential equation emerges as

$$\phi(x,y) = \sum_{n=1}^{N} \left\{ k_n \tan^{-1}\left[\left(y - \frac{y_n a^2}{x_n^2 + y_n^2} \right) \left(x - \frac{x_n a^2}{x_n^2 + y_n^2} \right)^{-1} \right] - k_n \tan^{-1}\left(\frac{y - y_n}{x - x_n} \right) \right\}, \tag{4}$$

Since $n \in [1, N]$, this formulation can be readily adapted to prescribe an arbitrary number of vortices by altering the upper bound on the summation term to reflect the number of induced vortices in a cylindrical chamber configuration.

Up to this point, the position of each vortex has been left arbitrary, so long as it satisfies the geometric requirement of being located within the cylindrical boundary given by $x_n^2 + y_n^2 < a^2$. However, Eq. (4) may be further reduced by applying the physical conditions associated with quad symmetry (for $N = 4$) in order to achieve a balanced quadrupole configuration, namely,

$$\begin{aligned} k_1 &= -k_2 = k_3 = -k_4 && \text{(counter-rotation, equal strength)} \\ x_1 &= -x_2 = -x_3 = x_4 && \text{(symmetry about the } y\text{-axis)} \\ y_1 &= y_2 = -y_3 = -y_4 && \text{(symmetry about the } x\text{-axis).} \end{aligned} \tag{5}$$

As for a hexapole, somewhat similar conditions apply, specifically,

$$\begin{aligned} k_1 &= -k_2 = k_3 = -k_4 = k_5 = -k_6 && \text{(counter-rotation, equal strength)} \\ x_1 &= -x_3 = -x_4 = x_6; \quad x_2 = x_5 = 0 && \text{(symmetry about the } y\text{-axis)} \\ y_1 &= y_3 = -y_4 = -y_6; \quad y_2 = -y_5 && \text{(symmetry about the } x\text{-axis).} \end{aligned} \tag{6}$$

Lastly, for an octopole, one can write,

$$\begin{aligned} k_1 &= -k_2 = k_3 = -k_4 = k_5 = -k_6 = k_7 = -k_8 && \text{(counter-rotation, equal strength)} \\ x_1 &= -x_4 = -x_5 = x_8; \quad x_2 = -x_3 = -x_6 = x_7 && \text{(symmetry about the } y\text{-axis)} \\ y_1 &= y_4 = -y_5 = -y_8; \quad y_2 = y_3 = -y_6 = -y_7 && \text{(symmetry about the } x\text{-axis).} \end{aligned} \tag{7}$$

In the interest of brevity, we focus on the quadrupole analysis whose equalities transform Eq. (4) into

$$\begin{aligned} \phi(x,y) = k_1 \Bigg\{ &- \tan^{-1}\left(\frac{y - y_1}{x - x_1} \right) + \tan^{-1}\left(\frac{y - y_1}{x + x_1} \right) - \tan^{-1}\left(\frac{y + y_1}{x + x_1} \right) + \tan^{-1}\left(\frac{y + y_1}{x - x_1} \right) \\ &+ \tan^{-1}\left(\frac{y - \Lambda y_1}{x - \Lambda x_1} \right) - \tan^{-1}\left(\frac{y - \Lambda y_1}{x + \Lambda x_1} \right) + \tan^{-1}\left(\frac{y + \Lambda y_1}{x + \Lambda x_1} \right) - \tan^{-1}\left(\frac{y + \Lambda y_1}{x - \Lambda x_1} \right) \Bigg\}, \end{aligned} \tag{8}$$

where $\Lambda \equiv a^2/(x_1^2 + y_1^2)$. With $\phi(x, y)$ in hand, the velocity components may be determined by taking

$$\begin{aligned} u_x = \frac{\partial \phi}{\partial x} = k_1 \Bigg[&\frac{y - y_1}{(x - x_1)^2 + (y - y_1)^2} - \frac{y - y_1}{(x + x_1)^2 + (y - y_1)^2} + \frac{y + y_1}{(x + x_1)^2 + (y + y_1)^2} \\ &- \frac{y + y_1}{(x - x_1)^2 + (y + y_1)^2} - \frac{y - \Lambda y_1}{(x - \Lambda x_1)^2 + (y - \Lambda y_1)^2} + \frac{y - \Lambda y_1}{(x + \Lambda x_1)^2 + (y - \Lambda y_1)^2} \\ &- \frac{y + \Lambda y_1}{(x + \Lambda x_1)^2 + (y + \Lambda y_1)^2} + \frac{y + \Lambda y_1}{(x - \Lambda x_1)^2 + (y + \Lambda y_1)^2} \Bigg] \end{aligned} \tag{9}$$

and

$$\begin{aligned} u_y = \frac{\partial \phi}{\partial y} = k_1 \Bigg[&- \frac{x - x_1}{(x - x_1)^2 + (y - y_1)^2} + \frac{x + x_1}{(x + x_1)^2 + (y - y_1)^2} - \frac{x + x_1}{(x + x_1)^2 + (y + y_1)^2} \\ &+ \frac{x - x_1}{(x - x_1)^2 + (y + y_1)^2} + \frac{x - \Lambda x_1}{(x - \Lambda x_1)^2 + (y - \Lambda y_1)^2} - \frac{x + \Lambda x_1}{(x + \Lambda x_1)^2 + (y - \Lambda y_1)^2} \\ &+ \frac{x + \Lambda x_1}{(x + \Lambda x_1)^2 + (y + \Lambda y_1)^2} - \frac{x - \Lambda x_1}{(x - \Lambda x_1)^2 + (y + \Lambda y_1)^2} \Bigg]. \end{aligned} \tag{10}$$

The same strategy may be extended straightforwardly to capture any number of even vortices.

C. Piecewise Helical Solution

To make further headway, we may follow the example of Park et al. [20] and patch a solid-body core over the vortex center to create a piecewise Rankine vortex [21]. The resulting vortices produce a velocity distribution that may be specified relative to the vortex centers according to:

$$u_r = 0, \quad u_\theta = kr/r_R^2; \quad r \le r_R \tag{11}$$

$$u_r = 0, \quad u_\theta = k/r; \quad r > r_R. \tag{12}$$

In reference to the origin of our reference frame, these expressions yield

$$u_x^{(\mathrm{i})} = k_n(y - y_n)/r_R^2, \qquad u_y^{(\mathrm{i})} = k_n(x - x_n)/r_R^2; \qquad \sqrt{(x - x_n)^2 + (y - y_n)^2} \le r_R \tag{13}$$

$$u_x^{(\mathrm{o})} = u_x, \qquad u_y^{(\mathrm{o})} = u_y; \qquad \sqrt{(x - x_n)^2 + (y - y_n)^2} > r_R, \tag{14}$$

where the pairs $(u_x^{(\mathrm{i})}, u_y^{(\mathrm{i})})$ and $(u_x^{(\mathrm{o})}, u_y^{(\mathrm{o})})$ refer to the inner and outer vortex segments of the piecewise vortex, respectively.

While the method of patching seems to be effective, certain precautions are necessary to ensure the validity of the model. Firstly, no vortex should be positioned within one core radius from the boundary in order to avoid possible interference from exterior singularities; furthermore, while oblique vortex collisions can be typically handled with acceptable accuracy, the inviscid nature of the solution allows for seemingly unrealistic collisions when adjacent vortices meet head-on. In practice, these restrictions do not prove to be too obtrusive, especially in what concerns the initial placement of the vortices. If, on the other hand, a dynamic simulation is attempted (as described below), a sufficiently fine mesh must be used in order for the model to accurately reconcile vortex collisions while overcoming the stopping criteria for the simulation. Naturally, the underlying assumption of uniform axial flow transforms the motion's dependence on time and space to a time-dependence only. This idealization, in turn, enables an iterative approximation of the velocity field down the bore. This may be achieved by computing the velocity of the vortex centers and incrementing the solution by a finite time step to calculate the new vortex location at a correspondingly small distance downstream.

D. Equilibrium Points

One of the primary motivations for starting with four vortices, when an arbitrary number can be described by Eq. (4), is the balanced nature associated with a multipole vortex configuration. Any even-numbered arrangement allows for each vortex to be bordered by a neighbor with opposite rotationality, which is essential to prevent the onset of imbalanced motion. Assortments of four, six, and eight poles in particular offer distinct advantages regarding the establishment and maintenance of the vortices. Specifically, there exists a set of equidistant equilibrium points about which the vortex centers tend to gyrate for a balanced group, when the circulation and spacing of each vortex is uniform as described by Eqs. (5–7). If initiated precisely at these points, each of the vortices will exert an influence on the others so that the resultant velocity at each vortex center is identically zero. In this case, the position of the vortices will remain fixed in time. If initiated in the vicinity of these equilibrium points, the vortices will gyrate around the point while remaining confined to their quadrants in a repeating pattern that is effectively neutrally stable. If the vortices are initiated too far from their equilibrium points, the configuration becomes unstable and the vortex centers will be seen to travel in increasingly wider paths around their quadrants until they are pushed up against the wall or each other.

Fortunately, the possession of a complete solution for the velocity field makes the derivation of these equilibrium points rather straightforward. Starting with either Eq. (9) or Eq. (10), the velocity can be equated to zero and the location of the vortices can be simplified for a balanced and equidistant configuration by setting $x = x_1$ and $y = y_1$. Assuming unit radius, solving for x_1 and y_1 returns the position of the equilibrium point(s). Reducing the resulting expression for $N = 4, 6$ and 8, one obtains the following values of (x_1, y_1) and (x_2, y_2), which appear separately in Eqs. (6) and (7):

$$N = 4 : (0.4188, 0.4188); \; N = 6 : (0.5717, 0.3301), (0, 0.6601); \; N = 8 : (0.6530, 0.2705), (0.2705, 0.6530). \tag{15}$$

In fact, these roots may be confirmed numerically to five decimal places using the code described in Sec. III. The latter solves Eq. (3) rather than Eqs. (9–10) while serving to provide an independent verification.

In practice, an optimum solution may be achieved by initializing the vortices near their equilibrium points using two, three, or four triangular vorticators that are evenly spaced for $N = 4, 6$, and 8, respectively. Such a configuration stands to maximize the coherence of the MpV structure while still alleviating the pitfalls of uneven fuel consumption.

III. Theoretical and Computational Results

A. Potential-Flow Simulations

The theoretical formulation of Sec. II.C is used to develop a MATLAB code that calculates and displays the velocity field. Forthwith, Fig. 3a showcases the results of a static simulation wherein the distances are normalized by the cylinder radius and velocities are normalized by the maximum initial velocity at the edge of each vortex core. The vortices are located at $(\pm 0.4, \pm 0.4)$ and have core radii of 0.2. For the creation of Fig. 3a, the mesh is specified by $\Delta x = \Delta y = 0.067$. Moreover, the non-dimensional value of the circulation is set to $\pm 2\pi$. The general pattern of the velocity field displays the expected behavior seen in experiments and CFD simulations, with stagnation points appearing at the center as well as along the wall at the vertical and horizontal extremes, where opposing vortices cancel.

Simulations show that a disturbance in the tangential direction, such as a single vortex that is initialized slightly out of place, will cause the vortices to rotate in unison around the axis of the chamber. In practice, their orbiting motion will promote circumferentially uniform burning and reduce sliver formation. A similar effect is engendered by the counter-rotating and spinning diamond-impregnated tricone roller bits used in the oil-extraction industry.

Evidently, imposing quad symmetry leads to highly stable and coherent vortices with favorable mixing characteristics. In the absence of viscous damping, however, and irrespective of the widely varying input values that we try, the results of our MATLAB simulations consistently predict a rotary motion of the poles that increases in both tangential speed and magnitude as the flow progresses downstream. This particular characteristic should produce an appreciable wall-abrasion effect when implemented in a hybrid rocket engine. Additionally, perturbing the initial location of one or more vortices by a small distance can be shown to produce continuing asymmetric behavior over time that is characterized by strong cellular rotation. Otherwise, the simulated vortex motion displays effective mixing characteristics with very stable, dynamic structures.

B. CFD Simulations

A simple CFD simulation using a finite volume solver [22] is used to verify the analytical solution. As depicted in Fig. 3b, our geometry consists of a right cylinder that is 5.08 cm in diameter and 38.1 cm long, with two open ends. A quad vortex motion is induced by inserting a pair of triangular vortex trippers into the flow at an aggressive 60 degrees angle of attack toward the inlet, particularly, as recommended by Dake and Majdalani [16]. Each vorticator consists of an isosceles triangle with a 2.54 cm base and a 1.9 cm height, thus subtending an apex angle of 67.4 degrees and two 2.29 cm sides. The base of each vorticator tab is positioned 5.08 cm downstream of the inlet.

The geometry is created using SolidWorks and imported into ANSYS Workbench for further processing. Surfaces are defined based on the imported geometry, and then discretized with an unstructured tetrahedral mesh. The default element size is 0.8 mm and the elements are permitted to grow to a maximum size of 0.16 cm at a growth rate of 1.2 mm. Overall, the mesh is very finely prescribed for the type of simulations being performed, with over 3.4 million tetrahedral elements that are reduced to approximately 634,000 polyhedral elements. Figure 3c provides some relevant geometric detail after meshing. As for the boundary conditions, they are imposed as follows: air with a uniform axial velocity of 1 m/s enters through the inlet while the outlet is set to atmospheric pressure. The simulation invokes the realizable $k - \varepsilon$ viscous model. These conditions allow for a comparison of the potential flow formulation described

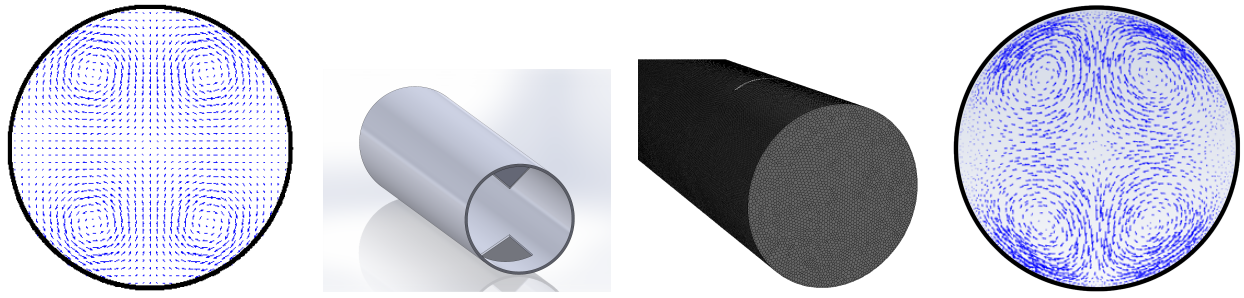

a) **b)** **c)** **d)**

Fig. 3. Simulation domains showing a) analytical QpV structure (potential flow model), b) chamber comprising two triangular vorticators, c) unstructured polyhedral mesh in use, and d) computed QpV structure [22].

in Sec. II to a viscous solution in Fig. 3d. Convergence of the simulation is quickly accomplished, with the continuity residual falling below 10^{-3}, after only 270 iterations. All other residuals are seen to fall below 5×10^{-5}.

The spiraling motion of the poles may be further illuminated by visualizing the flow in three-dimensional space. This is illustrated in Fig. 4a where the three-dimensional streamlines corresponding to Fig. 3d are displayed. Note that, with the sole exception of the centerline, all streamlines complete at least one helical rotation before reaching the aft end of the chamber. The evolution of a similar flow pattern, as shown in Fig. 4b, may be compared to the case associated with vortices being imposed in two tightly grouped pairs on opposing sides of the chamber (see Fig. 4c).

The data derived from CFD simulations is qualitatively compared to the results obtained using the potential flow model of a quadrupole in Fig. 5. The input parameters for the potential flow analysis are chosen to match the CFD solution at four radii from the headwall ($2a$ downstream of the vortex trippers) in order to establish a common initial

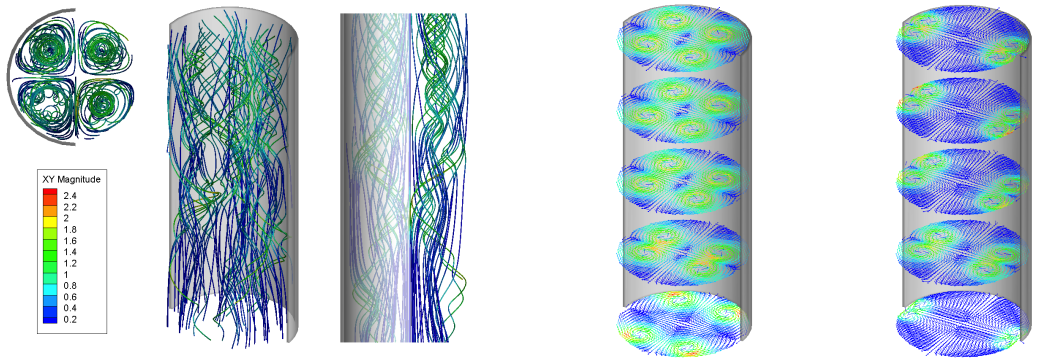

Fig. 4. CFD simulations showcasing a) typical streamlines associated with two triangular vorticators, b) initial velocity vectors leading to quad symmetry and c) streamwise evolution of vortices.

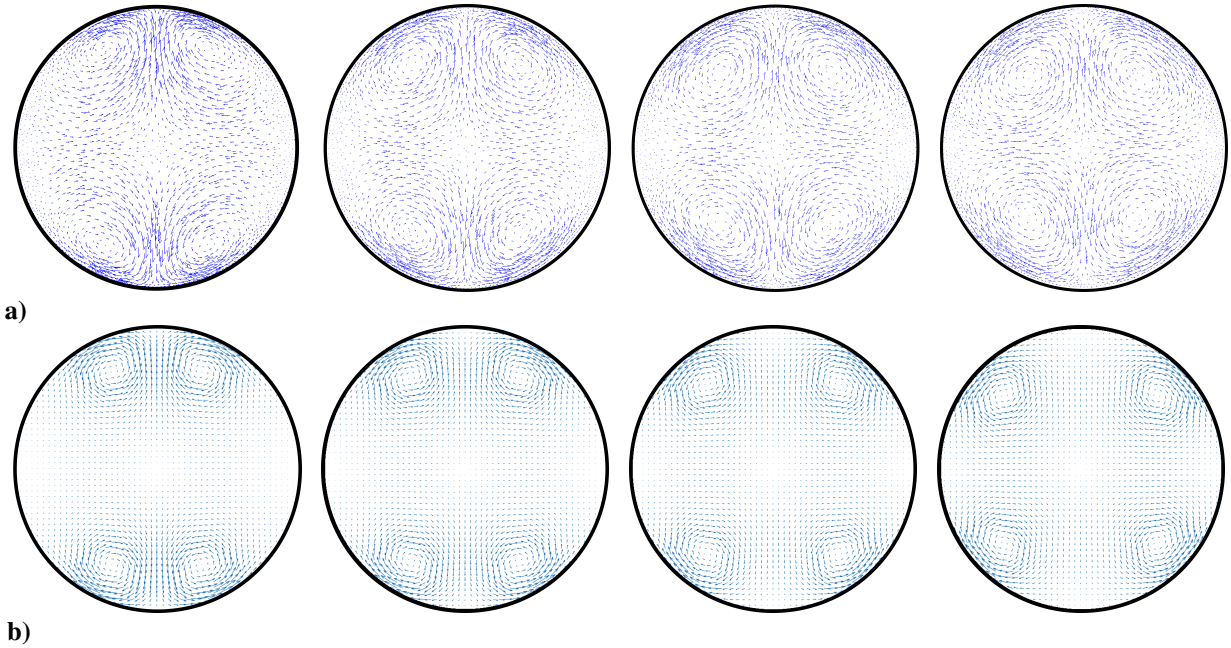

Fig. 5. Comparison between a) CFD results for a Quadrupole Vortex (QpV) configuration at four different axial stations of 4, 6, 8, and 10 radii from the headwall and b) corresponding potential flow predictions at the same locations. The MATLAB predictions are initialized 4 radii from the headwall with $r_R = 0.18a$, $\Gamma = \pm 2\pi/5$, and $z_n = (\pm 0.32a, \pm 0.75a)$.

condition. The potential flow model is then used to predict the flow velocities for the remainder of the engine, namely, at six, eight, and ten radii. Overall, the agreement may be considered to be quite satisfactory. The CFD solution generates vortices that are evenly paired and that move outward from their initial locations, namely, in good agreement with the MATLAB predictions. Moreover, the motion near the wall seems to agree quite well between the two cases in light of the opposing boundary conditions used consistently in each model. One key distinction can be made between the two models: transverse velocities in the CFD simulations exhibit definite axial decay as viscous forces act on the fluid. Whereas the theoretical vortices remain strong far downstream in the potential model, peak vortices occur near the middle of the chamber in the viscous simulations, where balance is struck between full development and eventual dissipation. The structure of the vortices remains coherent over nearly the entire length of the chamber, but the magnitude of the swirling velocity decays almost exponentially. Despite this expected difference, the potential flow model seems capable of capturing the essential bulk motion of four vortices gyrating within their respective quadrants with a reasonable degree of accuracy. In fact, the same level of agreement between theory and computations is achieved when the same analysis is repeated using hexapole and octopole vortex configurations, as showcased in Figs. 6 and 7.

C. Regression Rate Prediction

Procedurally, the regression rate improvement that can be expected from the use of a multipole vortex configuration may be roughly estimated based on the regression rate model developed by Marquardt [23]. According to these simulations, the fuel grain in a QpV engine with an equilibrium vortex placement will regress, on average, 46% faster than the non-swirling case. By switching the vortex placement to match that created by the triangular tabs of Sec. III.B, the improvement is increased to 59%.

It should be noted that the improvement in regression rate remains a function of the velocity that is evaluated at the boundary layer edge; the latter is approximated by its invisicid value at the wall. At each axial station in our regression rate solver, the xy planar velocities are computed. The magnitude of the transverse velocity along the wall is subsequently averaged to estimate the local swirl number. These values are then substituted into the main solver routine for the swirling regression rate model to deduce the regression rate, port diameter, mass flux, and so on, at each particular station. The 59% relative improvement may be confirmed by running a QpV case and comparing it to an axially injected motor of the same size and injection mass flux. In this context, doubling the number of vortex trippers to induce eight vortices (in lieu of four) will boost the regression rate by a factor of two (conservatively) because the

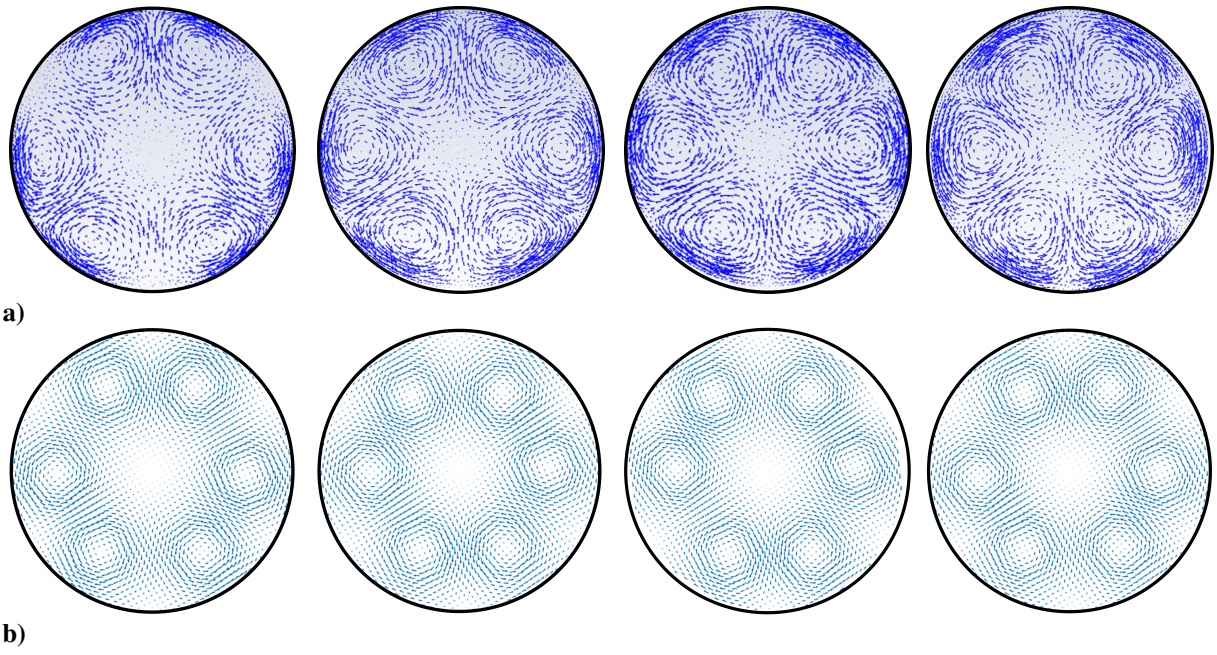

Fig. 6. Comparison between a) CFD results for a Hexapole Vortex (HpV) configuration at four different axial stations of 4, 6, 8, and 10 radii from the headwall and b) corresponding potential flow predictions.

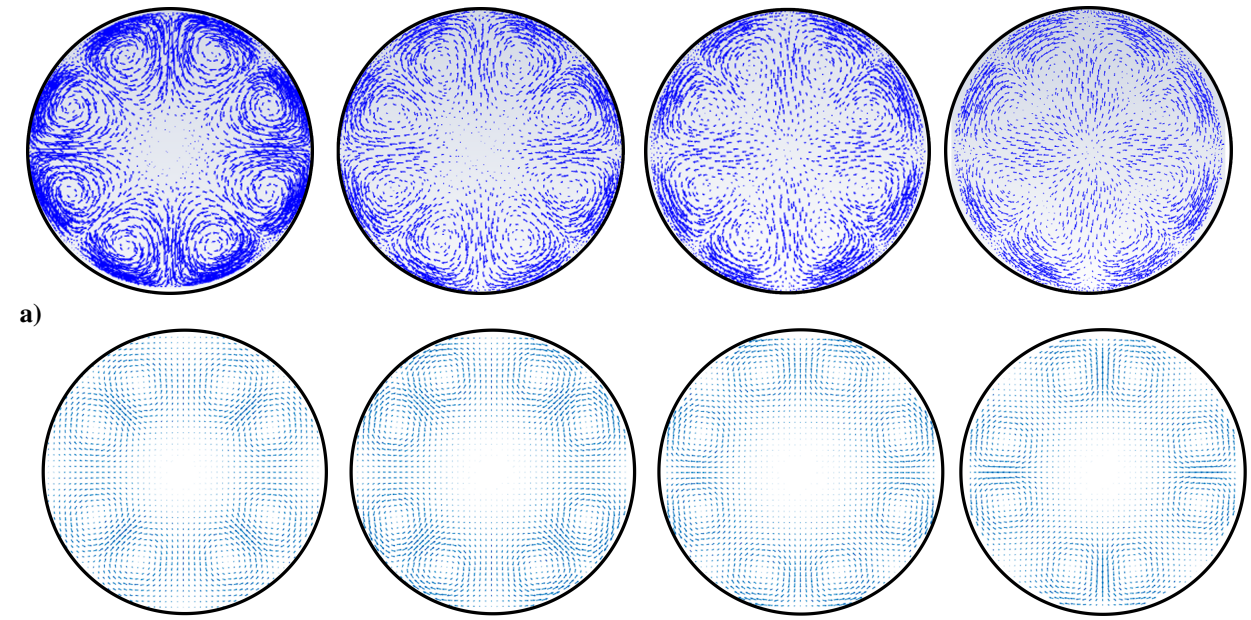

Fig. 7. Comparison between a) CFD results for an Octopole Vortex (OpV) configuration at four different axial stations of 4, 6, 8, and 10 radii from the headwall and b) corresponding potential flow predictions.

tab-induced vortices become smaller and closer to the wall. In the presence of two trippers and four vortices only, relatively larger gaps open up between the vortices, thus leading to much weaker wall velocities. Conversely, eight evenly distributed vortices are prone to fill the gaps much more efficiently to the extent of producing an estimated 120% increase in regression.

Another key takeaway is that vortex placement can appreciably affect the local (circumferential) burning trend in a manner that is reflective of the local velocity at the grain surface. Once again, the triangular vorticators produce a higher axially-averaged regression rate at the expense of a much less uniform burning profile. It thus seems viable to tailor the desired regression profile and rate of an MpV engine by prescribing the vortex strengths and positions, even though the two features remain coupled. If an even-burning grain is desired, then a stable or neutrally-stable vortex arrangement will likely produce the most desirable outcome. On the other hand, partially-symmetrical configurations such as those corresponding to the pattern created by pairs of opposed triangular tabs may have niche utility in non-circular ports. The inverse problem may also be solved: a knowledge of the flowfield created by the vortex generators will allow for the grain thickness to be customized to reduce sliver formation for any particular vortex arrangement.

Before leaving this subject, it may be instructive to note that the unique characteristics of the MpV flowfield have barely been explored in this non-reactive flow investigation. In particular, the fact that the flow scrapes against the walls with high localized velocities before turning inward and transporting combustion products to the core of the engine has implications beyond the destratification of the mixture temperature. It is possible that the rapid entrainment of gasses from the boundary layer into the center of the engine will include reactants as well as products, thus effectively creating the opportunity for reactions to unfold outside of a diffusion-limited environment. This behavior would represent a gaseous analog to the well-known droplet entrainment mechanism observed in paraffin fuels [24] to which their heightened regression rates have been ascribed. The unburned fuel in an MpV motor with sufficient vortex strength will convect to the core as a ready-to-burn gas with the available oxidizer in a kinetically-limited process that is no longer impeded by the slow rate of species diffusion or droplet evaporation. Meanwhile, reacting products from the hot central core region will continue to be brought into contact with the fuel grain in a strongly swirling vortex motion. It may be speculated that the intense mixing of oxidizer and fuel in the core region, coupled with the rapidly sweeping motion across the grain surface, can lead to much higher regression rates than reported here, namely, rates that are typically associated with a pre-mixed combustion process. From this perspective, a hybrid MpV engine can potentially offer regression rates that exceed the present diffusion-limited model predictions by an entire order of magnitude, i.e., rivaling the burning rates of solid rockets while retaining the unique benefits that hybrid concepts continue to offer.

IV. Conclusions

In this investigation, a velocity formulation for a multipole vortex (MpV) is systematically derived from first principles using the Milne-Thomson Circle Theorem. The resulting two-dimensional, potential flow solution confirms that an even set of vortices that are embedded within a cylindrical chamber can be rendered hydrodynamically stable. This stability suggests the viability of MpV configurations as an alternative to conventional unidirectional and bidirectional vortex injection schemes for hybrid rocket engines. A useful outcome of this analysis is the determination of the equilibrium points for multipole vortex systems. By furnishing both the velocity field and the equilibrium points, this study advances our understanding of the MpV flow topology. Our findings also facilitate qualitative assessments of the bulk gaseous motion and the rotational tendency of the vortices when initially displaced from their equilibrium positions. While the present formulation remains idealized, it constitutes a fundamental stepping stone toward a more comprehensive assessment of the MpV engine concept. Throughout this process, our numerical simulations seem reassuring as they exhibit favorable qualitative agreement with the analytical mean flow predictions. This concordance lends credence to the potential flow model's predictive utility within the expected constraints of the underlying assumptions, thereby reinforcing its applicability to real-world engine designs.

A retrospective application of the regression rate model developed by Marquardt [23] suggests that an MpV engine may produce a sizable enhancement in grain regression rate relative to a conventional hybrid engine. For the operating conditions and motor scale considered, the projected increase reaches approximately 120% conservatively for an Octopole Vortex (OpV) engine. Additional improvements may be anticipated from the vigorous recirculation of combustion products and destratification effects that remain intrinsic to the MpV configuration, although such benefits are yet be validated experimentally. Should the formation of coherent vortices through tangential injection be successfully demonstrated in a laboratory setting, the MpV paradigm could be exploited to augment regression rates in hybrid propulsion systems in a game-changing, highly customizable manner.

In complementing the work of Marquardt and Majdalani [15], the $N-$pole velocity formulation obtained in this study marks the first step in a broader sequence of investigations that can be aimed at refining our understanding of the hydrodynamic and thermal characteristics of multipole vortices. Future analysis may be directed more specifically toward: (i) extending the present formulation to account for viscous effects using matched-asymptotic expansions; (ii) deriving an analytical regression rate model that accommodates the sweeping motion of gases above the fuel surface and the non-uniformity of the flowfield; (iii) revising Marxman's diffusion-limited theory to incorporate three-dimensional flow effects; (iv) assessing the heat transfer enhancement induced by MpV motion through a combination of theoretical modeling, CFD simulations, and experimental validation; (v) examining the impact of chamber aspect ratio variations on MpV stability and performance; (vi) simulating the MpV structure under compressible reactive and non-reactive conditions; (vii) delineating the conditions conducive to MpV inception, precession, and breakdown; (viii) identifying and mitigating potential combustion instabilities associated with MpV development; and (ix) comparing the characteristics of MpV-assisted flowfields to those of cyclonic origin [15, 25–27].

From an even broader perspective, this work may be seen to support ongoing efforts at systematically characterizing swirl-driven hybrid rockets for the purpose of refining their predictive models and extending their parametric design optimization space. Owing to their inherent safety and adaptability for manned missions, hybrid rockets continue to offer a compelling alternative to solid and liquid rocket propulsion systems. However, their widespread integration remains predicated on sustained research to further improve their performance and expand their operational envelope. It is anticipated that the insights gained from this investigation will serve as a modest resource for researchers and engineers striving to advance hybrid rocket technology.

References

[1] Altman, D. and Humble, R., *Space Propulsion Analysis and Design*, McGraw Hill, 1995.

[2] Jens, E. T., Cantwell, B. J., and Hubbard, G. S., "Hybrid Rocket Propulsion Systems for Outer Planet Exploration Missions," *Acta Astronautica*, Vol. 128, 2016, pp. 119–130. doi:https://doi.org/10.1016/j.actaastro.2016.06.036.

[3] Majdalani, J., "Analytical Models for Hybrid Rockets," *Fundamentals of Hybrid Rocket Combustion and Propulsion*, edited by M. J. Chiaverini and K. K. Kuo, Progress in Astronautics and Aeronautics, Chapter 5. AIAA Progress in Astronautics and Aeronautics, 1801 Alexander Bell Drive, Reston, Virginia 20191-4344, 2007, pp. 207–246. doi:10.2514/5.9781600866876.0207.0246.

[4] Majdalani, J., "Vortex Injection Hybrid Rockets," *Fundamentals of Hybrid Rocket Combustion and Propulsion*, edited by M. J. Chiaverini and K. K. Kuo, Progress in Astronautics and Aeronautics, Chapter 6. AIAA Progress in

Astronautics and Aeronautics, 1801 Alexander Bell Drive, Reston, Virginia 20191-4344, 2007, pp. 247–276. doi:10.2514/5.9781600866876.0247.0276.

[5] Karabeyoglu, A., Zilliac, G., Cantwell, B. J., DeZilwa, S., and Castellucci, P., "Scale-Up Tests of High Regression Rate Paraffin-Based Hybrid Rocket Fuels," *Journal of Propulsion and Power*, Vol. 20, No. 6, Nov. 2004, pp. 1037–1045. doi:10.2514/1.3340.

[6] Knuth, W. H., Chiaverini, M. J., Gramer, D. J., and Sauer, J. A., "Experimental Investigation of a Vortex-Driven High-Regression Rate Hybrid Rocket Engine," *34th AIAA/ASME/SAE/ASEE Joint Propulsion Conference and Exhibit*, AIAA Paper 1998-3348, July 1998. doi:10.2514/6.1998-3348.

[7] Cantwell, B. J., "Similarity Solution of Fuel Mass Transfer, Port Mass Flux Coupling in Hybrid Propulsion," *Journal of Engineering Mathematics*, Vol. 84, No. 1, June 2013, pp. 19–40. doi:10.1007/s10665-013-9624-y.

[8] Ozawa, K. and Shimada, T., "Performance of Mixture-Ratio-Controlled Hybrid Rockets Under Uncertainties in Fuel Regression," *Journal of Propulsion and Power*, Oct. 2020, pp. 1–14. doi:10.2514/1.b37970.

[9] Knuth, W. H., Bemowski, P. A., Gramer, D. J., Majdalani, J., and Rothbauer, W. J., "Gas-Fed, Vortex Injection Hybrid Rocket Engine," SBIR Phase I, NASA Final Technical Contract No. NAS8-40679, Orbital Technologies Corporation, Madison, Wisconsin, Aug. 1996.

[10] Knuth, W. H., Chiaverini, M. J., Sauer, J. A., and Gramer, D. J., "Solid-Fuel Regression Rate Behavior of Vortex Hybrid Rocket Engines," *Journal of Propulsion and Power*, Vol. 18, No. 3, 2002, pp. 600–609. doi:10.2514/2.5974.

[11] Knuth, W. H., Chiaverini, M. J., Gramer, D. J., Sauer, J. A., Clair, C. P. S., Whitesides, R. H., and Dill, R. A., "Preliminary Computational Fluid Dynamics Analysis of the Vortex Hybrid Rocket Chamber and Nozzle Flowfield," *34th AIAA/ASME/SAE/ASEE Joint Propulsion Conference and Exhibit*, AIAA Paper 1998-3351, July 1998. doi:10.2514/6.1998-3351.

[12] Knuth, W., Gramer, D., Chiaverini, M., and Sauer, J., "Development and Testing of a Vortex-Driven, High-Regression Rate Hybrid Rocket Engine," *34th AIAA/ASME/SAE/ASEE Joint Propulsion Conference and Exhibit*, AIAA Paper 1998-3507, July 1998. doi:10.2514/6.1998-3507.

[13] Chiaverini, M. J., Malecki, M. J., Sauer, J. A., Knuth, W. H., and Majdalani, J., "Vortex Thrust Chamber Testing and Analysis for O2-H2 Propulsion Applications," *39th AIAA/ASME/SAE/ASEE Joint Propulsion Conference and Exhibit*, AIAA Paper 2003-4473, July 2003. doi:10.2514/6.2003-4473.

[14] Knuth, W. K., Sauer, J. A., Malecki, M. J., Hall, C. D., and Chiaverini, M. J., "Final Report on Vortex Universal Stoichiometric Preburner (VUSP) – A Phase I SBIR Project," SBIR Phase I, NASA Final Technical Contract No. NAS8-02021, OTC-GS0120-FR-02-1, Orbital Technologies Corporation, Madison, Wisconsin, May 2002.

[15] Marquardt, T. A. and Majdalani, J., "On the Quadrupole Vortex Motion in a Right-Cylindrical Hybrid Rocket Engine," *51st AIAA/SAE/ASEE Joint Propulsion Conference*, AIAA Paper 2015-3743, July 2015. doi:10.2514/6.2015-3743.

[16] Dake, T. J. and Majdalani, J., "Improving Flow Circulation in Heat Sinks Using Quadrupole Vortices," *ASME 2009 InterPACK Conference, Volume 2*, ASME, 2009. doi:10.1115/interpack2009-89211.

[17] Gak, M. Z., "Laboratory Investigation of a Self-Excited Oscillation in a System of Four Vortices," *Izvestiya, Atmospheric and Oceanic Physics*, Vol. 17, No. 2, 1981, pp. 147–150.

[18] Pleshanova, L. A., "Self Oscillations in a Four Vortex System," *Izvestiya, Atmospheric and Oceanic Physics*, Vol. 18, No. 4, 1982, pp. 263–269.

[19] Milne-Thomson, L. M., *Theoretical Aerodynamics*, St. Martins Press, New York, NY, 1966.

[20] Park, J., Heister, S. D., and Sullivan, J., "Development of a Counter-Rotating Vortex Pair (CVP) Mixer for Aerospace Applications," *49th AIAA/ASME/SAE/ASEE Joint Propulsion Conference and Exhibit*, AIAA Paper 2013-3832, July 2013. doi:10.2514/6.2013-3832.

[21] Rankine, W. J. M., *A Manual of Applied Mechanics*, Richard Griffin and Co., London, UK, 1858.

[22] ANSYS, "Fluent, Release 2020 R1, Version 18.1," 2020.

[23] Marquardt, T. A., *Characterization of Swirl-Driven Hybrid Rocket Engines*, Ph.D. dissertation, Auburn University, Department of Aerospace Engineering, December 2020.

[24] Karabeyoglu, M. A., *Transient Combustion in Hybrid Rockets*, Ph.D. dissertation, Stanford University, Department of Aeronautics and Astronautics, 1998.

[25] Majdalani, J., "Helical Solutions of the Bidirectional Vortex in a Cylindrical Cyclone: Beltramian and Trkalian Motions," *Fluid Dynamics Research*, Vol. 44, No. 6, Oct. 2012, pp. 065506–38. doi:10.1088/0169-5983/44/6/065506.

[26] Fleischmann, J. and Majdalani, J., "Complex Lamellar Helical Solution for Cyclonically Driven Hybrid Rocket Engines," *53rd AIAA Aerospace Sciences Meeting*, AIAA Paper 2015-0372, Jan. 2015. doi:10.2514/6.2015-0372.

[27] Marquardt, T. A. and Majdalani, J., "Beltramian Solution for Cyclonically Driven Hybrid Rocket Engines," *53rd AIAA/SAE/ASEE Joint Propulsion Conference*, AIAA Paper 2017-4638, July 2017. doi:10.2514/6.2017-4638.